Temporal dose inversion properties of adaptive biomolecular circuits

Eiji Nakamura[1], Franco Blanchini[2], Giulia Giordano[3], Alexander Hoffmann[4], and Elisa Franco[1*]

[1]Department of Mechanical and Aerospace Engineering, University of California, Los Angeles, USA
[2]Department of Mathematics, Computer Science and Physics, University of Udine, Italy
[3]Department of Industrial Engineering, University of Trento, Italy
[4]Department of Microbiology, Immunology, and Molecular Genetics, University of California, Los Angeles, USA
[*]Correspondence: efranco@seas.ucla.edu

SUMMARY

Cells have the capacity to encode and decode information in the temporal features of molecular signals. Many pathways, for example, generate either sustained or pulsatile responses depending on the context, and such diverse temporal behaviors have a profound impact on cell fate. Here we focus on how molecular pathways can convert the temporal features of dynamic signals, in particular how they can convert transient signals into persistent downstream events and vice versa. We describe this type of behavior as temporal dose inversion, and we demonstrate that it can be achieved through adaptive molecular circuits. We consider motifs known as incoherent feedforward loop (IFFL) and negative feedback loop (NFL), and identify parametric conditions that enable temporal dose inversion. We next consider more complex versions of these circuits that could be realized using enzymatic signaling and gene regulatory networks, finding that both circuits can exhibit temporal dose inversion. Finally, we consider a generalized IFFL topology, and we find that both the time delay in the inhibition pathway and the relative signal intensities of the activation and inhibition signals are key determinants for temporal dose inversion. Our investigation expands the potential use of adaptive circuits as signal processing units and contributes to our understanding of the role of adaptive circuits in nature.

KEYWORDS

temporal coding, pulse signaling, duration filtering, systems biology, incoherent feedforward loop

INTRODUCTION

Biological systems sense and respond to various physiological inputs, such as hormones, cytokines, and growth factors, by processing these signals through complex signaling pathways. These pathways lead to specific biological outcomes not only by producing or eliminating biomolecular components, but also by introducing temporal fluctuations of their concentration or activity[1–4]. A well-known example is the extracellular signal-regulated kinase (ERK), which can take different temporal characteristics and accordingly induce different biological outcomes in the mitogen-activated protein kinase (MAPK) network. ERK signals show either a transient or sustained behavior, depending on the input identity[5–7]. Epidermal growth factor (EGF) induces transient ERK activity, which triggers proliferation, whereas nerve growth factor (NGF) induces sustained ERK activity, which is translated to differentiation. ERK also plays an essential role in animal development. In the early Drosophila embryo, a high-dose ERK pulse induces gut endoderm differentiation, while a low-dose ERK pulse triggers cells to adopt neurogenic ectoderm[6]. The importance of temporal features has become evident in many biological contexts, including but not limited to neuronal activity[8] and hormonal signaling[9–11], leading to the notion of "temporal signaling" or "temporal coding" by which living organisms encode and interpret information based on the timing, duration, frequency, and amplitude of signals over time.

Here we consider a broad question pertaining to temporal coding: what signaling networks can enable cells to select transient inputs based on their duration and amplitude? It is known that sustained signals and transient signals can be discriminated by simple network motifs such as the incoherent feedforward

loop (IFFL) and the negative feedback loop (NFL)[12–17]. The IFFL and NFL are well-known for their adaptive behavior, which means they respond only transiently to changes in their input signal, typically taken to be a sustained amplitude input change. After a transient, the circuit eventually recovers its original state, unless the input perturbs the system beyond its tolerance. Intriguingly, we found that the IFFL and NFL can also produce a sustained output in response to a transient input, indicating their ability to discriminate inputs based on temporal features, and to process them to generate outputs with opposite temporal patterns.

Through computational simulations we systematically characterize how the IFFL and NFL motifs process transient input signals and invert their temporal features. We say a system presents temporal dose inversion if it produces a sustained output when stimulated with a short-lived input, and vice-versa produces a short-lived output in response to a sustained input, as illustrated in Figure 1. We measure the output response with two metrics: signal duration and temporal dose. Temporal dose is broadly intended as the area under the curve (AUC, i.e. the integral) of a transient signal, which depends on both its amplitude and its duration. Accordingly, we define two types of temporal dose inversion properties: inverse dose duration (IDD) and inverse dose AUC (IDA). An IDD circuit converts a short pulse into a longer pulse and vice versa, functioning as a duration inverter. An IDA circuit converts a small-AUC input into a large-AUC output and vice versa, functioning as a temporal dose amplifier. When a circuit specifically detects a transient signal, it is expected that the circuit shows the temporal dose inversion properties. Through computational methods, we characterize the temporal dose inversion properties of IFFL and NFL circuits by considering pulsatile inputs of varying duration, and derive parametric and topological conditions for implementing inversion properties.

The IFFL is a versatile motif that features one activation pathway and one inhibition pathway in parallel[16,18–22]. The behavior of the IFFL has typically been studied using step input functions: in this case, the expected response is a transient pulse owing to the presence of a delayed inhibition branch in the circuit[23,24]. The output initially increases and then is repressed, approaching an equilibrium that, in some cases, is identical or sufficiently close to its pre-stimulus state (perfect adaptation)[25]. Under certain assumptions, the output level directly depends on the ratio of the new input level to the pre-stimulus input level (fold-change detection)[26,27]. Furthermore, the IFFL has attracted growing interest as a circuit for processing dynamic signals, especially for detecting and decoding pulsatile signals[12–16]. Some of these studies (computational and experimental) demonstrated that the IFFL circuit or its variants, such as an interlocked IFFL[13,14], can be utilized as pulse detectors that respond to pulsatile inputs with specific temporal features. Finally, the IFFL can work as a band-pass circuit[13,28,29].

The NFL is a circuit motif with an inhibitory feedback loop, which is known as a core motif for generating pulses and oscillations in a variety of contexts, including the circadian clock[30], NF-κB signaling pathways[31], and the p53/Mdm2 network[32]. In addition, under certain conditions the NFL is known for its capability of adaptation and fold-change detection[33–36], both of which are essential for maintaining the robust operation of cellular functions in noisy environments.

We begin our study by considering simple IFFL and NFL circuit models to investigate the requirements for the temporal dose inversion property through numerical simulations. Next, we examine more complex models meant to capture enzymatic signaling and gene regulatory networks, verifying that temporal dose inversion still occurs. Finally, we consider a generalized IFFL architecture that is parameterized by the length of the inhibition pathway, showing that delayed inhibition is essential for temporal dose inversion. We finally derive insights that help us understand how and to what degree we can control the duration threshold of the detected input pulse using an IFFL-based pulse detector, pointing to potential bioengineering and synthetic biology applications of temporal dose inversion.

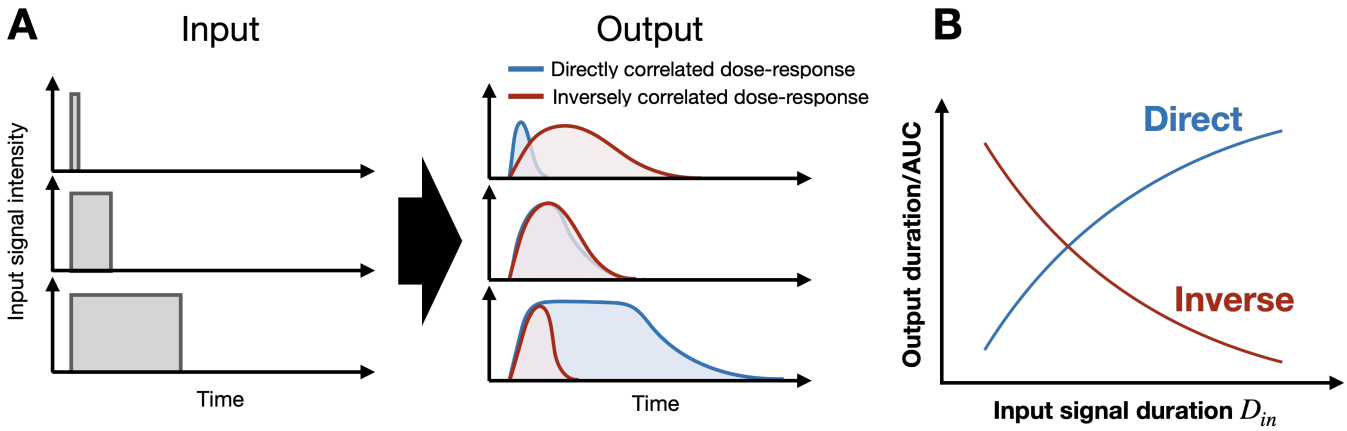

Figure 1: Temporal dose inversion in biomolecular circuits. (A) Illustrations of input-output circuit behaviors that maintain or invert the input temporal dose. (B) In a directly correlated dose-response, the output dose increases as input dose increases. In an inversely correlated dose response, the output duration decreases as the input dose increases.

RESULTS

1 Simple IFFL and NFL models illustrate the temporal dose inversion property

Numerous models have been proposed to describe IFFL-based circuits[26,37–39]. Here, we adopt the typical circuit topology of an IFFL composed of an input signal U, an intermediate chemical species X and an output chemical species Y (Figure 2A). We use lowercase letters to indicate concentrations; u is the amplitude of input signal U, and x and y represent the concentrations of the species X and Y respectively. Temporarily denoting the input amplitude by $\bar{u}$, we introduce a simple model to describe the IFFL as follows:

$$\frac{dx(s)}{ds} = \alpha\bar{u}(s) - \beta x(s) \tag{1}$$

$$\frac{dy(s)}{ds} = \gamma\bar{u}(s) - \delta x^p(s)y(s) - \epsilon y(s) \tag{2}$$

where α and γ are the input activation rate constants for species X and Y, respectively; β and ϵ are self-degradation rate constants for species X and Y, respectively; δ is the rate constant associated with inhibition of Y mediated by X, and p represents the order (i.e., cooperativity) of the reaction, while s is the time variable. We note that it is essential for our model to be nonlinear, as linear systems do not admit temporal dose inversion (Supplemental information).

To reduce the number of parameters, we rescale time in Equations 1 and 2, obtaining the updated model, which we will analyze in the following without loss of generality:

$$\dot{x}(t) = u(t) - x(t) \tag{3}$$

$$\dot{y}(t) = au(t) - bx^p(t)y(t) - cy(t) \tag{4}$$

where $t = \beta s$, $u = \alpha\bar{u}/\beta$, $a = \gamma/\alpha$, $b = \delta/\beta$ and $c = \epsilon/\beta$, while $\dot{x}(t) = \frac{dx(t)}{dt}$ and $\dot{y}(t) = \frac{dy(t)}{dt}$. Using Equations 3 and 4, we can evaluate the circuit dynamics with respect to parameters a, b, c, and p. We examine the response of the model to a rectangular input function of finite duration D_{in} with amplitude u_0:

$$u(t) = \begin{cases} u_0 & 0 \le t \le D_{in} \\ 0 & t > D_{in} \end{cases} \tag{5}$$

For the NFL, we adopt the simple circuit topology (Figure 2B) and obtain the corresponding equations with rescaled time as follows:

$$\dot{x}(t) = y(t) - x(t) \tag{6}$$

$$\dot{y}(t) = au(t) - bx^p(t)y(t) - cy(t) \tag{7}$$

The detailed derivation of Equations 6 and 7 is described in STAR Methods 3. The only difference from the IFFL model is that the first term of Equation 6 is $y(t)$ instead of $u(t)$. Throughout numerical simulations using these IFFL and NFL models, the initial conditions are $x(0) = 0$ and $y(0) = 0$. Responses of the simple IFFL model and the simple NFL model for different input durations D_{in} (from 0.2 to 1.0) are evaluated with $a = 2$, $b = 20$, $c = 0.1$, and $p = 2$ (Figure 2C and 2D).

The IFFL exhibits a long-lasting response to a shorter input duration (e.g. $D_{in} = 0.2$), and thus shows the capacity for inverse dose duration (IDD). To quantitatively evaluate its temporal dose inversion properties, we computed the output duration D_{out} and the area under the curve (AUC). D_{out} is calculated as the square root of the variance in the time domain, where the variance is derived as the difference between the second moment ($\int_0^\infty t^2 y(t)dt / \int_0^\infty y(t)dt$) and the square of the mean ($\int_0^\infty ty(t)dt / \int_0^\infty y(t)dt$). This approach is analogous to the calculation of the standard deviation in probability distributions. AUC is the integration of the output signal $y(t)$ from $t = 0$ to $t = 80$, as described in detail in STAR Methods 3. D_{out} and AUC are evaluated as a function of D_{in} (Figure 2E). D_{out} monotonically decreases as D_{in} increases: D_{out} and D_{in} are inversely correlated, and therefore the system has the inverse dose duration (IDD) property. Conversely, AUC increases when $0 < D_{in} < 0.25$, has a peak at $D_{in} = 0.25$, and decreases when $D_{in} > 0.25$. Hence, we argue that the IFFL exhibits the inverse dose AUC (IDA) property just in a range of D_{in} values ($D_{in} > 0.25$). The NFL circuit also exhibits IDD, as D_{out} is monotonically decreasing with respect to D_{in}, while it does not exhibit IDA, since AUC increases for increasing D_{in} (Figure 2D and 2F). We will compare the likelihood of the IDA property for IFFL and NFL in Section 2.

To understand how each parameter affects the circuit dynamics, we individually reduce and increase a, b and c by one order of magnitude with respect to their nominal value, in two different scenarios with input durations $D_{in} = 0.1$ and $D_{in} = 1$ (Figure 3). The activation parameter a mostly changes the amplitude of the output, without significantly affecting its duration. The inhibition parameter b and the degradation parameter c change the output response more drastically. As b or c increases, the output duration decreases, because a larger value of b or c brings the output level more quickly back to its basal level. However, when $D_{in} = 1$, the output duration does not perceptibly decrease as c increases; this happens because, owing to the longer input duration, the effect of the inhibition term $bx^p y$ is dominant.

To systematically investigate how each parameter affects the temporal dose inversion property of the IFFL circuit, D_{out} and AUC are displayed as heat maps in the D_{in}-a, D_{in}-b, D_{in}-c and D_{in}-p planes (Figure 4). Here, D_{in} is linearly varied from 0.1 to 1 in steps of 0.05. The inversion properties of the circuits can be evaluated using these heat maps. When there is a cross-section at a specific value of a circuit parameter (e.g., $b = 20$ in the left middle panel of Figure 4B) along which D_{out} decreases (at least for a certain interval of D_{in} values), the circuit exhibits the IDD property for a set of specific parameter values. Similarly, when we find a cross-section at a specific value of a circuit parameter along which AUC decreases (at least for a certain interval of D_{in} values), the circuit exhibits the IDA property for a set of specific parameter values. The IFFL shows both the IDD and IDA properties within a certain range of each parameter (Figure 4A and 4B). While the activation parameter a does not change D_{out} (and therefore does not affect the IDD property), a higher value of a favors an apparent IDA property. The inhibition parameter b and the degradation parameter c significantly affect both D_{out} and AUC; as b or c increases, the circuit dynamics accelerates, which can be seen in the fact that the region with large D_{out} expands as b or c decreases. The dependence of AUC on b is more complicated than that of D_{out}. Although AUC increases as b decreases because of a smaller inhibition effect, decreasing b leads to the loss of the IDA property: for instance, along a cross-section with $b = 2$ (Figure 4B middle), AUC monotonically increases as D_{in} increases (hence, there is no IDA property). Therefore, b should not be too small to obtain the IDA property at least for a range of D_{in} values, whereas a larger value of a and lower value of c are preferable to ensure the IDA property at least in some ranges of D_{in}.

The NFL can also exhibit the IDD and IDA properties, but for a smaller set of parameters with respect to the IFFL (Figure 4C). Concerning the IDD property, differently from the IFFL circuit, the NFL shows

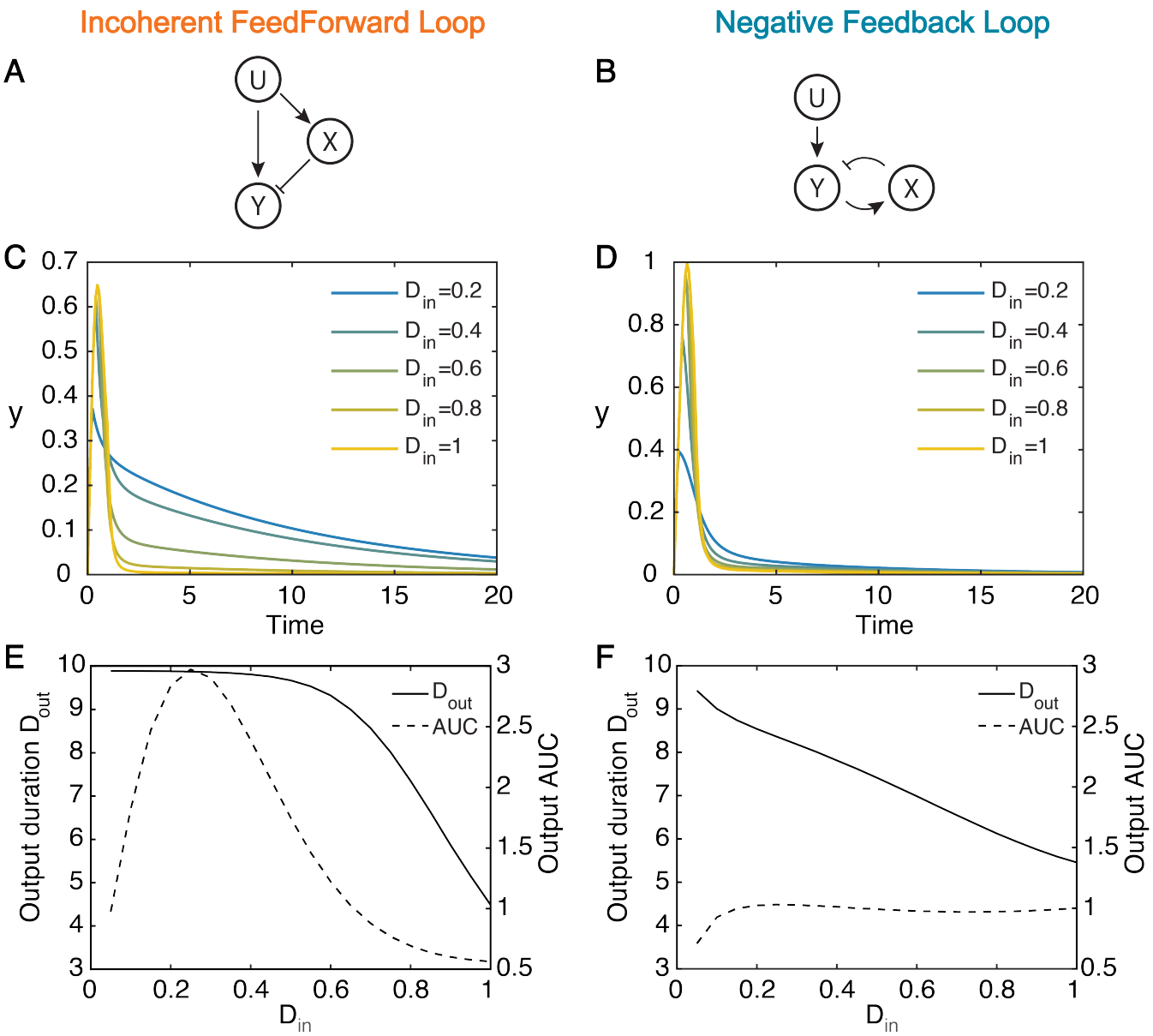

Figure 2: Our simple models for the incoherent feedforward loop (IFFL) and the negative feedback loop (NFL) circuits exhibit the temporal dose inversion property. (A,B) Circuit diagrams of (A) IFFL and (B) NFL. (C,D) Responses of (C) IFFL and (D) NFL to pulsatile inputs with varied duration D_{in} from 0.2 to 1.00, with $a = 2$, $b = 20$, $c = 0.1$, and $p = 2$. (E,F) Input duration versus output duration or output AUC for (E) IFFL and (F) NFL, with D_{in} in the range from 0.05 to 1.00.

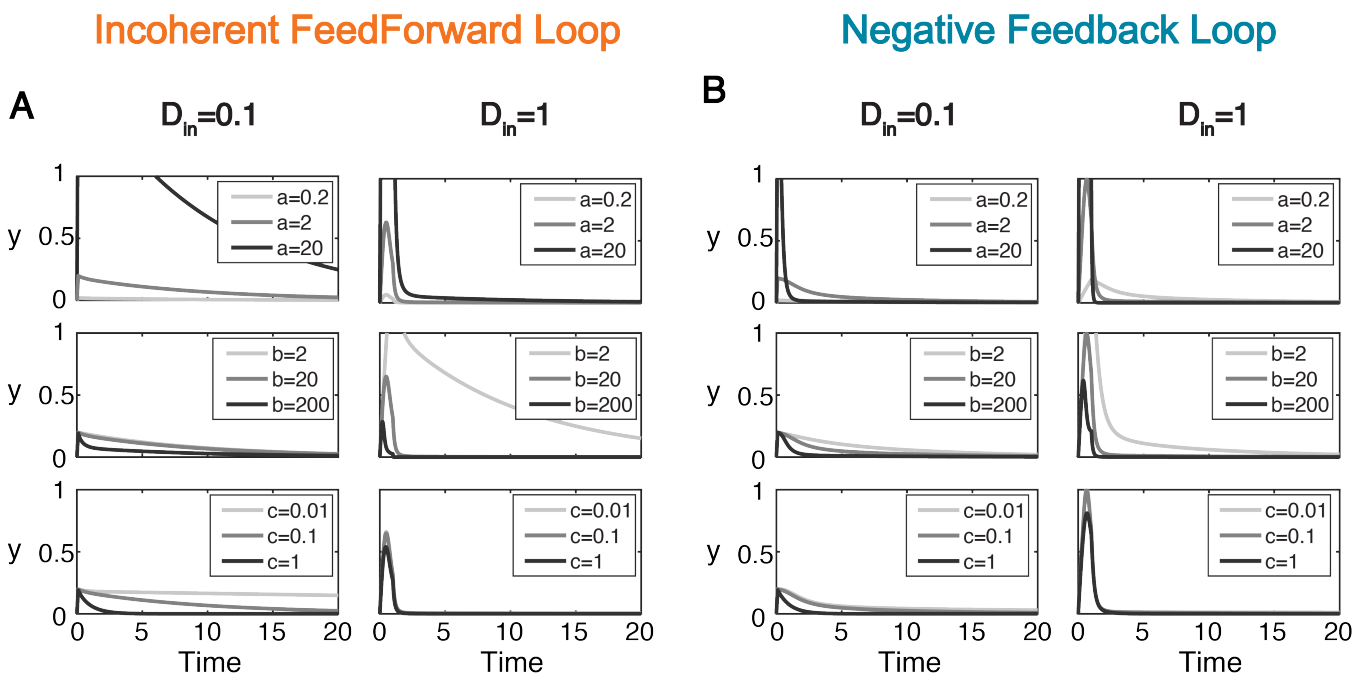

Figure 3: Evaluating the influence of individual parameter variations on the temporal response of the IFFL and NFL circuits. Temporal responses of (A) the IFFL and of (B) the NFL circuit to a rectangular input with amplitude $u_0 = 1$ when $D_{in} = 0.1$ (left) and when $D_{in} = 1$ (right). The values of varying parameters are indicated in the legends. All other parameters are kept constant at their nominal value $a = 2$, $b = 20$, $c = 0.1$, $p = 2$.

a strong dependence on the activation parameter a; in fact, the inhibitory feedback from X has to be triggered by Y and a determines how quickly Y activates X, which eventually affects D_{out}. Concerning the IDA property, it is worth pointing out that the color scales of the heat maps in Figure 4C (right) are smaller than those in Figure 4B (right), suggesting that, in the NFL, it is more difficult to identify a cross-section at a parameter value along which we see an apparent IDA property. Here is an explanation as to why the IFFL is more likely to exhibit the IDA property. In the IFFL, the activation and inhibition pathways can be tuned independently, so we can choose the parameters so that the output node Y is immediately activated, while X is activated with a certain (tunable) delay. Therefore, if D_{in} is smaller than a threshold, input U only activates Y, without activating the inhibition signal from X. Once D_{in} exceeds the threshold, both the activation and inhibition pathways are triggered, which eventually decreases AUC. This is the mechanism that allows us to attain the IDA property in the IFFL. In contrast, in the NFL, the activation pathway and the inhibition pathways acting on Y are not independent, and are stimulated simultaneously in most cases; in fact, it is relatively difficult to find a condition in which only Y is activated, keeping the inhibition feedback from X not significantly stimulated, because active Y stimulates X. This does not mean that the NFL does not exhibit the IDA property for any choice of the parameters, but provides us with a qualitative understanding of why IFFL is more likely than NFL to exhibit the IDA property.

We also investigate how parameter p, the order of the inhibition term, affects the IDD and IDA properties of the IFFL and NFL. D_{out} and AUC are shown as heat maps in the D_{in}-u_0 plane (Figure 5). It is worth noticing that all heat maps are symmetric with respect to the diagonal line in the D_{in}-u_0 plot (which is not the bisector, since the two axes have different scales). This suggests that, in order to change the input dose, varying the input amplitude u_0 is equivalent to varying the input duration D_{in}, and leads to the same temporal dose inversion property.

For both IFFL and NFL, the IDD and IDA properties are reinforced as p increases, namely, the ranges of D_{in} and u_0 where an apparent inverse relationship occurs expand. When $p = 3$, both the IFFL and NFL do not exhibit the IDD and the IDA properties for small u_0 (such as $u_0 = 0.5$), while they do exhibit the properties for larger u_0. This happens because, when $x < 1$, the inhibition term $bx^p y$ decreases as p

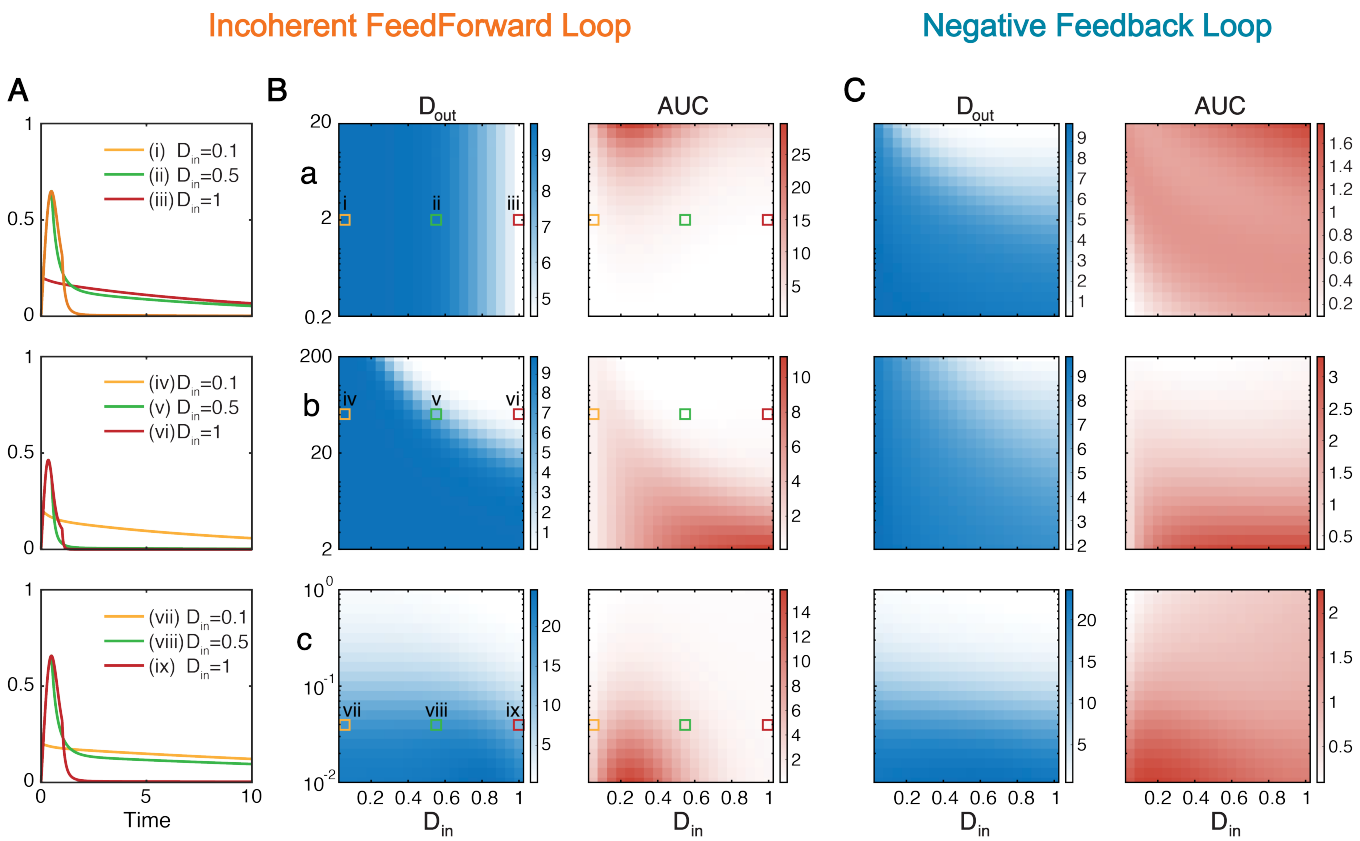

Figure 4: Evaluating the inverted dose-response as a function of individual parameters related to output production (a), inhibition (b), and degradation (c). (A) Time evolution of the output y with $D_{in} = 0.1$, $D_{in} = 0.5$, $D_{in} = 1$. Each output curve corresponds to the data point indicated with the same Roman numeral in the heat maps in panel B. (B,C) Heat maps showing the values of D_{out} (blue heat maps) and AUC (red heat maps) for the outputs of the IFFL (B) and the NFL (C) in the D_{in}-a, D_{in}-b, D_{in}-c planes respectively. In the same row or the same column, heat maps have the same axes units (only shown in the leftmost or bottom panels). Each row shows heat maps for a different parameter: a, top; b, center; c, bottom.

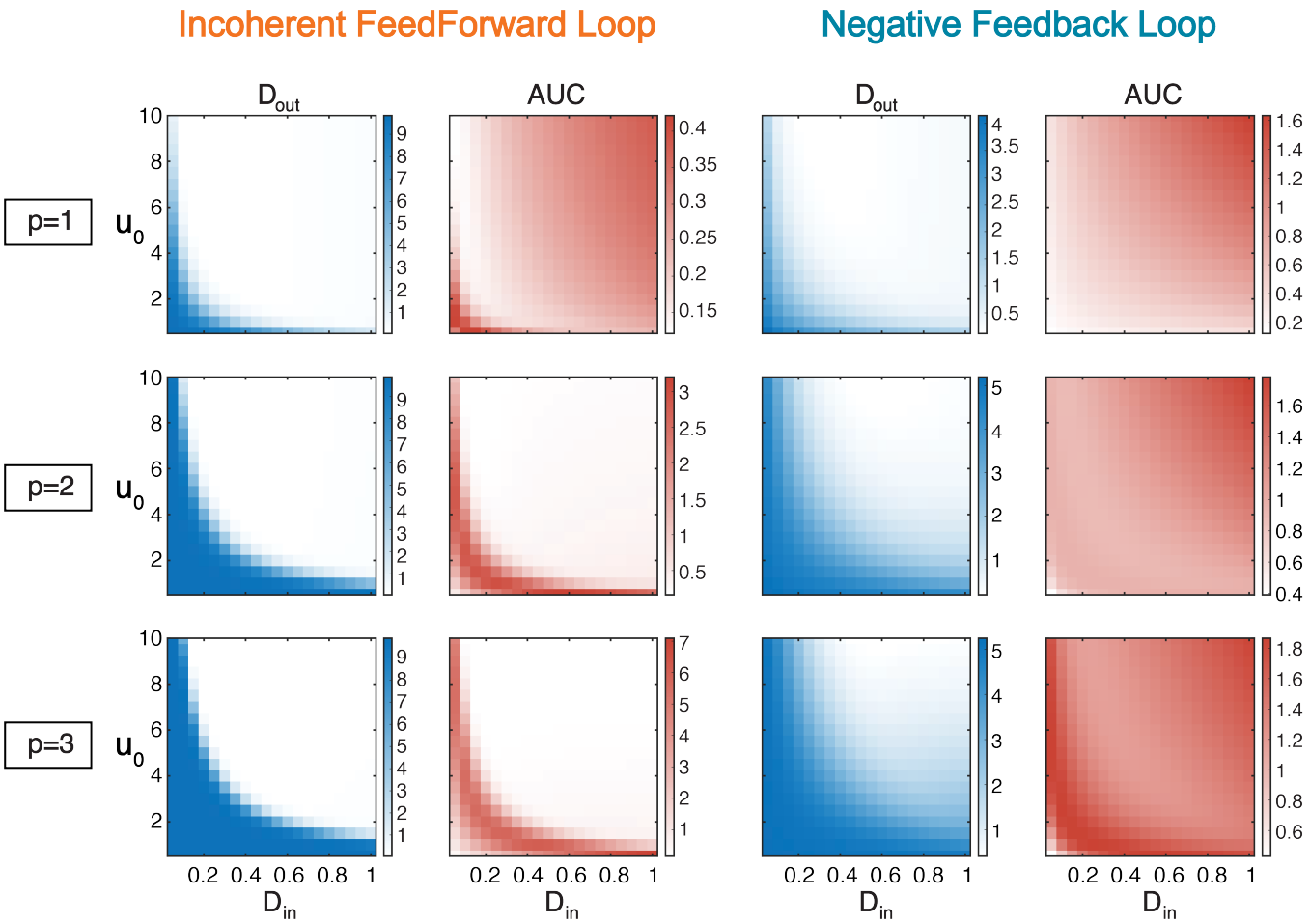

Figure 5: The higher order of the inhibition reaction reinforces the temporal dose inversion property. Heat maps showing the dependence of the IDD and IDA properties of the IFFL and NFL circuits on the cooperativity parameter p. For each circuit, the values of the output D_{out} (left) and AUC (right) are shown in the D_{in}-u_0 plane. In the same row or the same column, heat maps have the same axes units (only shown in the leftmost or bottom panels). Each row shows heat maps for different p values.

increases. For the IFFL, in the presence of an input signal, x (starting from the initial condition $x(0) = 0$) increases monotonically and asymptotically reaches its equilibrium value $x_{eq} = u_0$, which is obtained by solving Equation 3 with $\dot{x} = 0$ and $u(t) \equiv u_0$. Therefore, if $u_0 < 1$, then it is always $x(t) < 1$, which reduces the effect of the inhibition term $bx^p y$. However, as long as $u_0 > 1$, the degree p of the inhibition term reinforces the IDD and IDA properties.

2 Comparison of IFFL and NFL in terms of Inverse Dose-Response property using biological circuit models

To test whether the temporal dose inversion property can occur in more complex networks, we now consider more detailed IFFL and NFL models derived based on enzymatic signaling and gene regulatory networks (GRN).

Our signaling model for the IFFL is based on the work by Gerardin et al.[40]:

$$\dot{x}(t) = \alpha_x \frac{u(t)[1 - x(t)]}{K_{M,ux} + u(t) + [1 - x(t)]} - \gamma_x \frac{p_x x(t)}{K_{M,px} + p_x + x(t)}, \tag{8}$$

$$\dot{y}(t) = \alpha_y \frac{u(t)[1 - y(t)]}{K_{M,uy} + u(t) + [1 - y(t)]} - \beta_y \frac{x(t)y(t)}{K_{M,xy} + x(t) + y(t)} - \gamma_y \frac{p_y}{K_{M,py} + p_y + y(t)}. \tag{9}$$

All reactions assume enzymatic signaling and involve two species, X and Y, and one input, U. Each species is either in an active or inactive state. Activation and deactivation are scaled by reaction parameters α and β; K_M parameters are Michaelis-Menten constants; p_x and p_y are the concentrations of two basal deactivators, while γ_x and γ_y are the corresponding deactivation rate constants. Subscripts indicate the species associated with a particular parameter: for example, α_x is the activation rate constant of X and $K_{M,xy}$ is the Michaelis-Menten constant of enzyme X acting on substrate Y. To simplify the model, we assume that the total concentration of each species is conserved and normalized to 1. Further, we assume total quasi-steady-state approximation (tQSSA), which is valid for a wider range of parameter spaces than the conventional QSSA[41].

The gene regulatory network (GRN) model of the IFFL is as follows:

$$\dot{x}(t) = \delta_x \frac{[u(t)/K_{D,ux}]^{h_{ux}}}{1 + [u(t)/K_{D,ux}]^{h_{ux}}} - \epsilon_x x(t) \tag{10}$$

$$\dot{y(t)} = \delta_y \frac{[u(t)/K_{D,uy}]^{h_{uy}}}{1 + [u(t)/K_{D,uy}]^{h_{uy}} + [x(t)/K_{D,xy}]^{h_{xy}}} - \epsilon_y y(t) \tag{11}$$

where x and y denote concentrations of proteins (transcription factors). Parameters δ are maximal activation rates, while rate constants ϵ are associated with protein dilution/degradation. K_D is the dissociation constant and h is the Hill coefficient of a transcription factor from its target promoter.

The ODEs for the enzymatic signaling model and the gene regulatory model for the NFL are shown in STAR Methods 3.

We examine the response of these four models to a rectangular input function as in Equation 5, with a constant amplitude $u_0 = 0.5$ and varying duration D_{in}, and we evaluate the likelihood of the IDD or IDA properties for each circuit. The initial conditions are $x(0) = 0$ and $y(0) = 0$. We randomly choose 5000 parameter sets from a uniform distribution in the parameter ranges specified in STAR Methods 3 and reported in Table 1, and count the parameter sets for which the system exhibits the IDD or IDA property. To quantitatively assess the IDD and the IDA property, we calculate an IDD score (S_{IDD}) and an IDA score (S_{IDA}) as follows. Given an input duration interval $D_{in,1} < D_{in} < D_{in,2}$ for which the function $D_{out}(D_{in})$ has a negative derivative,

$$S_{IDD} = \frac{D_{out}(D_{in,1})}{D_{out}(D_{in,2})} - 1. \tag{12}$$

If there are multiple input duration intervals in which the function $D_{out}(D_{in})$ has a negative derivative, we choose our score S_{IDD} as the maximum value of $\frac{D_{out}(D_{in,1})}{D_{out}(D_{in,2})} - 1$. If the function $D_{out}(D_{in})$ is monotonically

increasing or constant, $S_{IDD} = 0$, which means that no IDD property is observed in the considered parameter set. S_{IDA} is computed analogously for the function $AUC(D_{in})$. By computing S_{IDD} and S_{IDA} values for each parameter set, we can quantify to which degree the IDD and IDA properties hold within that parameter set. More details on the mathematical computation of S_{IDD} and S_{IDA} are provided in STAR Methods 11.

Histograms of the IDD and IDA scores for each IFFL and NFL model are shown (Figure 6). The height of a bar in each histogram indicates the number of parameter sets that showed the corresponding positive IDD or IDA score. Regarding the IDD property, IFFL and NFL show a similar behavior: the signaling model is very likely to exhibit IDD (in 2671 cases out of 5000, for the IFFL, and 3091 cases out of 5000, for the NFL), whereas the GRN model exhibits IDD just for a small number of parameter sets (72 out of 5000, for the IFFL, and 53 out of 5000, for the NFL) and all the corresponding positive IDD score values are very small. Therefore, only the signaling models exhibit the IDD property within the evaluated parameter ranges. The IFFL signaling model is much more likely to exhibit the IDA property (in 213 cases out of 5000) than the NFL signaling model (in 28 cases out of 5000), again because of the independent activation and inhibition pathways. These results are consistent with those obtained using the simple models.

The GRN models for both IFFL and NFL have very few parameter sets associated with positive IDA scores (data not shown). A possible explanation as to why the GRN model does not exhibit the inversion properties is that the inhibitory interaction reduces the production rate of the output species, instead of eliminating the output species; also, after the input signal is removed, the decay dynamics mainly relies on the degradation rate that does not depend on X. For the gene expressing Y, it is assumed that each of the two transcription factors U and X independently binds to its specific target promoter domain[42]. If we introduced an inhibitory term based on protein-protein interactions, such as dephosphorylation and molecular sequestration, the model could show the inversion properties more frequently. Another possible reason is that we adopted the simplest GRN model without time delay, especially for translation. If we allow additional intermediate nodes to introduce additional time delay in the GRN model, the IDD and IDA properties can be achieved (Figure S 9).

3 Signal amplification and time delay affect the temporal dose inversion property

Our findings reveal that IFFL models show the IDA property more frequently than NFL models. So far, we have investigated the minimal IFFL model. Here, we study a more general form of IFFL to assess whether the temporal dose inversion property depends on topological constraints, and in particular on pathway length. This more general model also helps us to understand how IFFL-like signaling pathways with multiple intermediate species can show the temporal dose inversion property. We evaluate the circuit exclusively in terms of IDA, which is significantly more likely for the IFFL compared with the NFL (while we concentrate on IDA to streamline the discussion, the analysis can be readily extended to IDD using the same methods). The mathematical model of the generalized IFFL circuit is:

$$\dot{x}_1(t) = \alpha_{x_1}\frac{u(t)[1-x_1(t)]}{K_{M,ux}+u(t)+[1-x_1(t)]} - \gamma_{x_1}\frac{p_{x_1}x_1(t)}{K_{M,px}+p_{x_1}+x_1(t)} \tag{13}$$

$$\dot{y}_1(t) = \alpha_{y_1}\frac{u(t)[1-y_1(t)]}{K_{M,uy}+u(t)+[1-y_1(t)]} - \gamma_{y_1}\frac{p_{y_1}y_1(t)}{K_{M,py}+p_{y_1}+y_1(t)} \tag{14}$$

$$\dot{x}_i(t) = \alpha_{x_i}\frac{x_{i-1}(t)[1-x_i(t)]}{K_{M,x_i}+x_{i-1}(t)+[1-x_i(t)]} - \gamma_{x_i}\frac{p_{x_i}x_i(t)}{K_{M,px_i}+p_{x_i}+x_i(t)} \quad (i=2,3,...,m) \tag{15}$$

$$\dot{y}_j(t) = \alpha_{y_j}\frac{y_{j-1}(t)[1-y_j(t)]}{K_{M,y_j}+y_{j-1}(t)+[1-y_j(t)]} - \gamma_{y_j}\frac{p_{y_j}y_j(t)}{K_{M,py_j}+p_{y_j}+y_j(t)} \quad (j=2,3,...,n) \tag{16}$$

$$\dot{z}(t) = \alpha_z\frac{x_m(t)[1-z(t)]}{K_{M,xz}+x_m(t)+[1-z(t)]} - \beta_z\frac{y_n(t)z(t)}{K_{M,yz}+y_n(t)+z(t)} - \gamma_z\frac{p_z z(t)}{K_{M,pz}+p_z+z(t)} \tag{17}$$

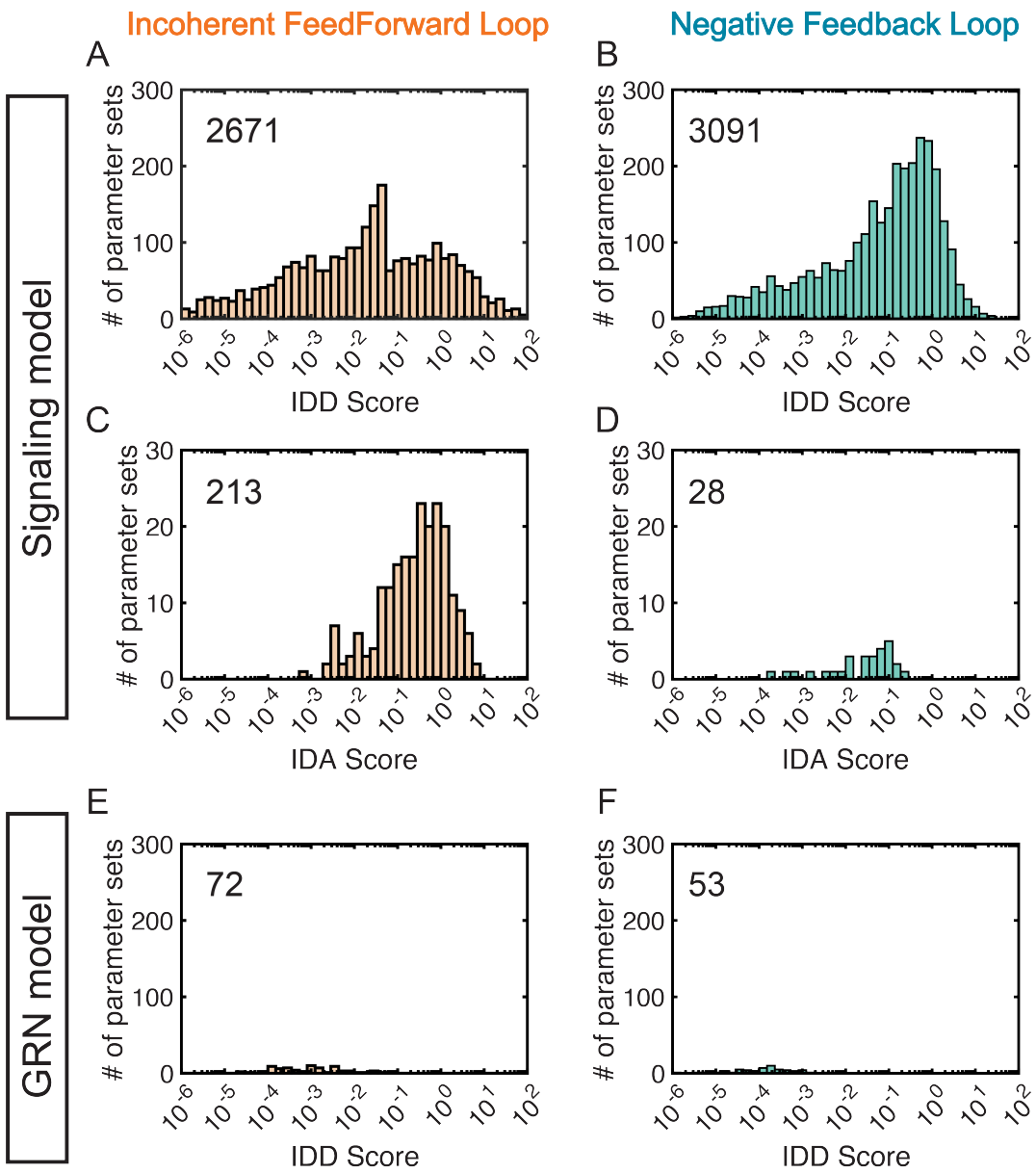

Figure 6: The IDA property is more likely to emerge in the IFFL motif. Histograms of IDD and IDA scores for 5000 randomly-chosen parameter sets. Each parameter is chosen from a uniform distribution in the interval specified in STAR Methods 3. For the IFFL signaling model, (A) IDD score histogram and (C) IDA score histogram. For the NFL signaling model, (B) IDD score histogram and (C) IDA score histogram. (E, F) IDD score histograms of gene regulatory model of the (E) IFFL and (F) NFL; IDA scores for these circuits are not shown because a negligible number of parameter sets present a positive score.

where m and n are the numbers of intermediate nodes in the activation pathway and the inhibition pathway, respectively, while the other parameters are labeled as in the IFFL signaling model in the previous section. To simplify the analysis, we assume $\alpha_{x_i} = \alpha_{y_j} = \alpha_x$ for all i and j. The initial conditions of all variables are set to zero.

We investigate how the intensity balance and the time delay between activation and inhibition determine the IDA property (Figure 7). IDA scores are computed from numerical simulations, and are visualized as heat maps in the m-n plane, for various choices of α_x and α_y (Figure 7). In particular, circuits with different values of the basal deactivation rates γ_{y_j} are considered (Figure 7A, 7B, and 7C. We only consider the nominal values for α_z and β_z and focus on the effects of the intermediate node parameters; the effects of varying α_z and β_z are shown in the Supplementary Figure 10.

In the case where $\gamma_{y_j} = 1$ for all $j \in \{1, 2, \ldots, n\}$, $m < n$ is required to have a non-negligible IDA score (Figure 7A). Since $m < n$ causes a delay in the inhibition pathway, a short input duration D_{in} does not induce a significant inhibition, while it still perceptibly activates the output, thus resulting in a higher IDA score. As long as $m < n$, though, further increasing the length n of the inhibition pathway is not always an advantage. For instance, when $a_y = 2$, the inhibition pathway shows signal amplification (that is, the activity level increases as the signal is transmitted through the inhibition pathway), and hence a longer pathway causes the inhibition effect to be stronger than activation, regardless of the value of D_{in}; therefore, in these cases, the IDA score decreases as n increases beyond a certain threshold (which is $n = 4$ when $m = 1$). A stronger inhibitory effect thus leads to the emergence of an optimal length of the inhibition pathway, given the length of the activation pathway.

We also consider the case with $\gamma_{y_j} = 0.1$ for all $j \in \{1, 2, \ldots, n\}$, corresponding to slow decay dynamics for all the nodes in the inhibitory pathway, which overall yields a long-lasting inhibition effect (Figure 7C). Consequently, the IDA score is negligible when $n \geq 2$, i.e., the pathway is too long. Also, being the inhibition already strong, the cases $a_y = 1$ and $a_y = 2$ show no apparent difference. Hence, similarly to the case (A) with $a_y = 2$ (Figure 7A), an excessively strong inhibition effect makes a too long inhibition pathway undesirable. When $a_x = 2$, the optimal length of the activation pathway is $m = 3$ (Figure 7C). The Supplementary Figure 8B shows the circuit dynamics, with $n = 1$, for different choices m. When $m = 1$, the output response to an input signal with small D_{in} (i.e. a shorter signal) lasts longer, with slowly decaying amplitude; conversely, the output response to an input signal with large D_{in} (i.e. a longer signal) is shorter and returns sooner to its basal level, which leads to a relatively small AUC. When $m = 3$, the output response to a shorter signal lasts longer (even though with an amplitude that is smaller than in the case $m = 1$), while the output response to a longer signal is much shorter and returns much sooner to its basal level than in the case $m = 1$, which eventually gives the maximum IDA score. When $m = 6$, the output response to a shorter signal lasts longer, but with an amplitude that is much smaller than in cases $m = 1$ and $m = 3$ and decays much faster, while the output response to a longer signal is even shorter, but initially has a very large amplitude, and therefore the IDA score is lower. The visualization of the time evolution of the signals helps understand why, for the circuit with $\gamma_{y_j} = 0.1$ for all $j \in \{1, 2, \ldots, n\}$ (Figure 7C), there is a value of m that maximizes the IDA score.

The previous cases show that activation and inhibition pathways with comparable intensities promote higher IDA scores (Figure 7A and 7C). If the activation is too strong, both small and large D_{in} values produce output responses with a long duration and a large amplitude, which lowers the IDA score. If the inhibition is too strong, both small and large D_{in} values produce output responses with small AUC values, which also lowers the IDA score. In a parameter space where the activation and inhibition intensities are relatively similar, we see a more complex pattern, showcased in the case with $\gamma_{y_1} = 0.1$ $\gamma_{y_j} = 1$ for $j \in \{2, \ldots, n\}$ (Figure 7B), which illustrates an intermediate configuration between Figure 7A and Figure 7C. When examining Figure 7 A through C, we observe that areas with high IDA scores shift closer to the x-axis and Figure 7B has the broadest areas with high IDA score. The same trend can also be observed when comparing the top panels ($a_x = 2$) and bottom panels ($a_x = 1$) in Figure 7B, that is, areas with high IDA score shift to the x-axis panels as a_x decreases (i.e., as the inhibition effect relatively increases). Eventually, among the four heat maps in Figure 7B, the lower right panel (with $a_x = 2$, $a_y = 1$) shows the broadest area with high IDA score. These findings exemplify that an optimal balance between the activation and inhibition pathways has to be satisfied to obtain the IDA property.

Finally, Figure 7D to G present numerical simulations with a set of specific parameters that yields

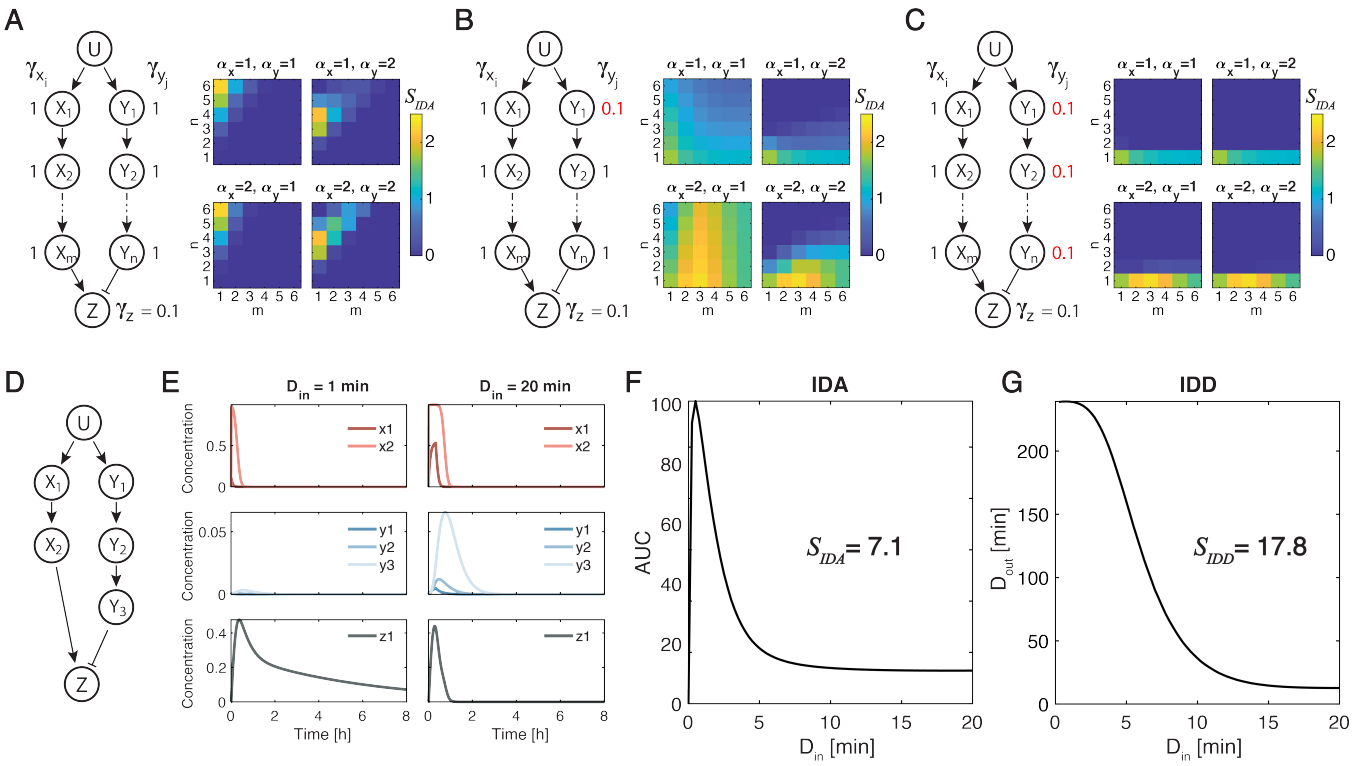

Figure 7: Generalized IFFL circuits show that the temporal dose inversion property depends on the relative strength of activation and inhibition pathways. (A to C) Each panel shows the circuit diagram of a generalized IFFL network, along with heat maps of IDA scores S_{IDA} in the m-n plane for different values of α_x and α_y, reported above each heat map. The basal deactivation rates are reported next to each node in the circuit diagram: in all three cases, $\gamma_{x_i} = 1$ for all $i = 1, \ldots, m$, and moreover (A) $\gamma_{y_j} = 1$ for all $j = 1, \ldots, n$; (B) $\gamma_{y_1} = 0.1$, and $\gamma_{y_j} = 1$ for $j = 2, \ldots, n$; (C) $\gamma_{y_j} = 0.1$ for all $j = 1, \ldots, n$. When not varied, the parameters are kept constant at their nominal values: $\alpha_z = 100$, $\beta_z = 10$, $\gamma_z = 0.1$, $K_{M,x} = K_{M,y} = K_{M,z} = 1.0$, $p_x = p_y = 1.0$, $p_z = 0.2$, $u_0 = 0.1$; D_{in} is logarithmically varied from $D_{in} = 0.1$ to $D_{in} = 10$. (D to G) An example of a circuit with a remarkably high IDA score. (D) Circuit diagram of a generalized IFFL network with $m = 2$ and $n = 3$. (E) Time evolution of the output responses of the circuit shown in (D) to two different input durations: $D_{in} = 1$ min (left), and $D_{in} = 20$ min (right) with the following parameters: $\alpha_{x_1} = \alpha_{x_2} = 50$, $\alpha_{y_1} = 0.5$, $\alpha_{y_2} = 1.5$, $\alpha_{y_3} = 2.5$, $\alpha_z = 5$, $\beta_z = 5$, $K_{M,x_1} = K_{M,x_2} = 1$, $K_{M,y_1} = K_{M,y_2} = K_{M,y_3} = 5$, $K_{M,xz} = 100$, $K_{M,yz} = 1$, $\gamma_{x_1} = \gamma_{x_2} = 0.5$, $\gamma_{y_1} = \gamma_{y_2} = \gamma_{y_3} = \gamma_z = 0.1$, $p_{x_1} = p_{x_2} = p_{y_1} = p_{y_2} = p_{y_3} = p_z = 0.3$, $u_0 = 0.005$. Plots of AUC as a function of D_{in} (F) and D_{out} as a function D_{in} (G) obtained from numerical simulations. D_{in} was linearly increased from 0 to 20 minutes with steps of 0.25 min. Note that $D_{out}(D_{in} = 0)$ is not included in the plot (G) because $D_{in} = 0$ gives $y(t) = 0$, with which D_{out} can not be calculated by Equation 35.

significantly high IDA and IDD scores ($S_{IDA} = 7.1$, $S_{IDD} = 17.8$). The parameter values, reported in the caption of Figure 7, have been chosen after a random parameter search; therefore, we cannot argue that this parameter set is the one that maximizes the IDA score. When $D_{in} = 1$ min, X_2 is immediately activated, but Y_3 is not substantially activated, and hence the output signal is long-lasting with large amplitude. Conversely, when $D_{in} = 20$ min, both X_2 and Y_3 are significantly activated, resulting in a pulse with a slightly smaller amplitude and a much shorter duration. The circuit showed a similar response to an even longer input duration $D_{in} = 100$ min (data not shown). Based on these features, we argue that the IFFL functions as a dose filter, meaning that it can selectively respond to transient signals (e.g., square-wave functions) or produce distinct output responses based on the nature of the input (pulsatile vs. sustained)[12–16].

Strictly speaking, the circuit in Figure 7D is a band-pass filter, in the sense that AUC as a function of D_{in} attains a maximum between $D_{in} = 0$ and $D_{in} = 1$, because the circuit does not produce any output if $D_{in} = 0$ (i.e., if there is no input signal). When the input amplitude u_0 is varied instead of D_{in}, $AUC(u_0)$ and $D_{out}(u_0)$ behave analogously to $AUC(D_{in})$ and $D_{out}(D_{in})$ (data not shown). Therefore, this circuit behaves as a band-pass filter with respect to both D_{in} and u_0. This observation is consistent with previous studies reporting that the IFFL circuit can implement a band-pass function and thus detect a certain range of the input dose by producing a larger steady-state response for a certain dose range of a sustained input[13,28,29,43,44].

DISCUSSION

We investigated the ability of IFFL and NFL circuits to process temporal information in input signals and to exhibit temporal dose inversion properties, specifically "Inverse Dose Duration" (IDD) and "Inverse Dose AUC" (IDA). Using simple models, we illustrated that both IFFL and NFL motifs are likely to exhibit IDD, but the IFFL is much more likely to exhibit IDA than the NFL. This trend was maintained when considering more complex signaling models with the same regulatory topology. A prominent difference between IFFL and NFL circuits is that, while the activation and inhibition pathways in the IFFL can be independently tuned, the inhibition pathway in the NFL circuit is automatically activated once the output node is activated; this explains why the NFL model is less likely to exhibit IDA, which requires stimulating only the activation pathway with a lower dose. We found that IFFL models based on enzymatic signaling interactions as well as gene network interactions exhibit IDD and IDA, and IDA occurs for a broad range of parameter values in the enzymatic IFFL models, demonstrating that it is a robust and controllable property. Finally, we investigated a particular IFFL enzymatic signaling model that shows a remarkably high IDA score, which suggests its usefulness as a dose filter.

Our finding that the IFFL motif acts as a dose filter aligns with several studies suggesting its capacity to detect pulsatile signals[12–16]. However, no prior work has systematically investigated how dose-response inversion can arise, and how it can be used to detect pulses. Additionally, it is important to note that the pulse detection principles outlined in previous work differ from those we identified here. For example, Lormeau et al.[14] showed that a single pulse can be detected using an interlocked IFFL circuit, and Benzinger et al.[13] showed how repeated pulsatile signals (i.e., pulse trains) can be detected using a diamond-shaped IFFL. Both studies rely on the falling-edge detection function of IFFL topologies. In this mechanism, while the input signal is present, the output remains minimal or absent because the input simultaneously activates both the activation and inhibition pathways. When the input disappears, the output increases due to the slower decay of the activation signal. In contrast, in our case the output response appears immediately after an input signal is applied, and disappears when the inhibition pathway takes over. Because the inhibition pathway requires a certain input dose to be activated, a shorter input duration or a smaller amplitude stimulates the output response more effectively. Thus, dose filtering emerges as a consequence of temporal dose inversion. A similar scheme was adopted for detecting pulse trains in[16], but their model assumed an extremely high Hill coefficient, which limits the applicability of their model.

The capacity of IFFL motifs for temporal dose inversion can be compared to their band-pass filtering properties, as explored in previous work[28,29,44,45]. In band-pass filtering, the IFFL thresholds for the activating and inhibiting pathways are independently calibrated. By setting the activation threshold to be

lower than the inhibition threshold, an IFFL circuit detects a specific range of the input concentration. In contrast, we define the temporal dose inversion property as detecting a dose based on its temporal evaluation. Through computational simulations, we also found a "duality" between IDD and IDA, illustrated in Figure 4C: IDD emerges when the input duration changes while the amplitude is constant, and IDA emerges when the input duration is constant while the amplitude changes. A consequence of this duality means that the dose filtering property mentioned earlier can be converted to either duration filtering or amplitude filtering when the input amplitude or input duration remain constant respectively. The duality helps explain why the IFFL motif finds broad utility beyond temporal signal processing (e.g., duration filtering). For example, Basu et al.[28] and Gao et al.[29] demonstrated the spatiotemporal patterning of cells taking advantage of the band-pass functionality (or the IDA property) of IFFL motif; their IFFL-like circuits can detect a spatial domain in which the concentration (i.e., amplitude) of a molecule of interest is within a certain range, which eventually lead to spatial patterning of bacterial colonies[28] and mammalian cells[29].

The concept of temporal dose inversion may provide a tool to describe and interpret behaviors observed in natural living systems which have been associated to temporal coding[4,46]. For example, tumor necrosis factor (TNF)-induced NF-κB signaling has been reported to exhibit behavior that appears consistent with a temporal dose inversion property, because it depends on the temporal properties of TNF pulses. First, TNF stimulates both the pro-apoptotic caspase pathway and the pro-survival NF-κB-driven gene transcription pathway. In turn, the pro-survival signal inhibits some steps in the pro-apoptotic caspase signaling. Therefore, if we view TNF as an input, and apoptotic cell death as an output, this pathway has a topology consistent with the IFFL motif. Lee et al.[47] reported that a 1-min TNF pulse induced apoptotic cell death more effectively than a 1-hour TNF pulse. How the pro-apoptotic pathway processes the temporal features of the TNF signal may be captured by the concept of the temporal dose inversion property. Furthermore, living cells interpret multiple combined features of temporally varying inputs, such as amplitude, duration, and frequency[3]. The exploration of input inversion properties could provide insights into how nature accomplishes this.

The temporal dose inversion property could be easily tested through experimental validation using artificial gene networks, paving the way for the development of complex temporal coding networks in synthetic biology. Numerous *in vitro* systems could be immediately adopted for this purpose, including gene networks in synthetic cells[48], artificial genelets, which have been already used to build individual or interconnected IFFLs[20], or the PEN toolbox[49]. Ultimately, these demonstrations could advance synthetic protein-level signaling systems that can process and decode pulses[44,50,51].

Another potential extension of the present study is the application of temporal dose inversion circuits to expand and simplify the combinatorial recognition of multiple temporal features of a signal, akin to the functionalities of living systems. For example, Benzinger et al.[13] demonstrated signal processing based on the amplitude and duty cycle of a pulse train, using two readouts. Through temporal dose-response inversion, it will be more straightforward to design circuits that detect duty cycle or perform even more intricate temporal signal processing. This direction of research helps us understand the mechanism of the temporal codes of cell signaling and provides us with sophisticated control of engineered biological systems. A rich library of artificial temporal codes allows us to expand our knowledge of molecular communication, and find potential applications for diagnostics[52], therapeutics[53],and material development[54].

Supplemental information

Linear systems do not exhibit temporal dose inversion

We consider causal linear time invariant systems with input $u(t)$ and state/output $y(t)$, characterized by a non-negative impulse response function $h(t)$. This class of systems is relevant to our study, because any physically plausible biological model must present non-negative variables at all times.
Assume $y(0) = 0$ and $u(t) = 0$ for $t \leq 0$. The forced response of this type of system is:

$$y(t) = \int_0^t h(t-\tau)u(\tau)d\tau.$$

Now consider a finite-duration step input $u_T(t)$:

$$u_T(t) = \begin{cases} 1 & 0 \leq t \leq T, \\ 0 & \text{otherwise.} \end{cases}$$

We find:

$$y_T(t) = \begin{cases} \int_0^t h(t-\tau)u_T(\tau)d\tau = \int_0^t h(t-\tau)d\tau & 0 \leq t \leq T, \\ Y_T L(t-T) & t > T, \end{cases}$$

where $Y_T = \int_0^T h(t-\tau)d\tau$ and $L(t)$ is the fundamental solution. If the system is stable, $L(t) < 1$ component-wise and $L(t) \to 0$ for $t \to \infty$.

Now consider two inputs u_{T_1}, u_{T_2}, with $T_1 < T_2$. Because the system has a positive impulse response, it must be that:

$$Y_{T_1} = \int_0^{T_1} h(t-\tau)d\tau < \int_0^{T_2} h(t-\tau)d\tau = Y_{T_2}$$

For any time t with $T_1 \leq t \leq T_2$, we have:

$$y_{T_1}(t) = Y_{T_1} L(t-T_1),$$
$$y_{T_2}(t) = \int_0^t h(t-\tau)d\tau.$$

Then because $L(t) < 1$, it must be true that $y_{T_1}(t) \leq y_{T_2}(t)$. This can be trivially extended to any time $t \geq T_2$. This means the magnitude of the response $y(t)$ scales with the duration of the input signal. In other words, this kind of system does not admit temporal dose inversion.

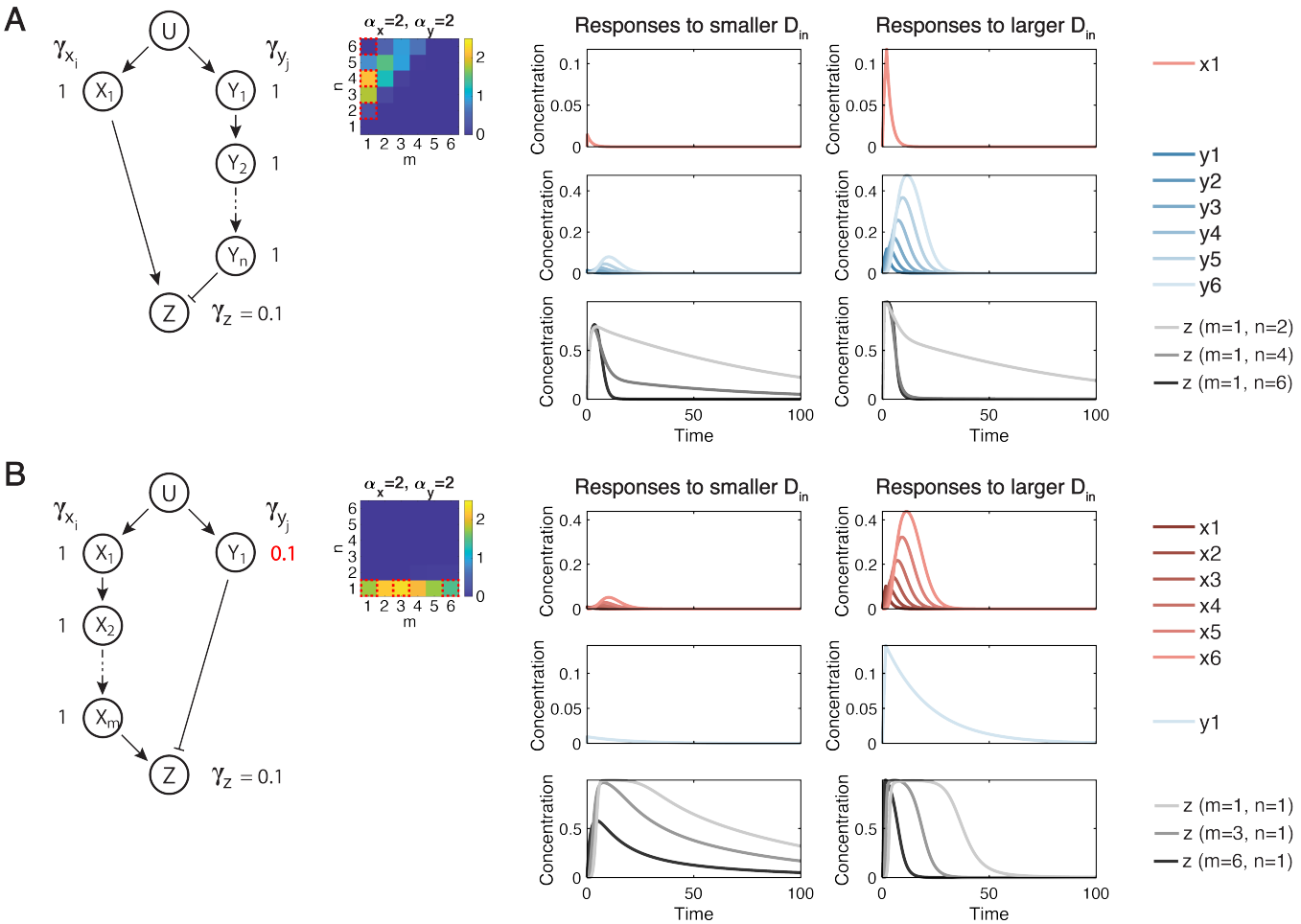

Figure 8: Dynamics of the circuit associated with the model in Equations 13-17 with different combinations of (m, n). (A) Behaviour of the circuit in Figure 7A, having $\gamma_{y_j} = 1$ for all j, with $m = 1$ and different values of n. (B) Behaviour of the circuit in Figure 7C, having $\gamma_{y_j} = 0.1$ for all j, with $n = 1$ and different values of m.

A GRN circuit showing the IDA property

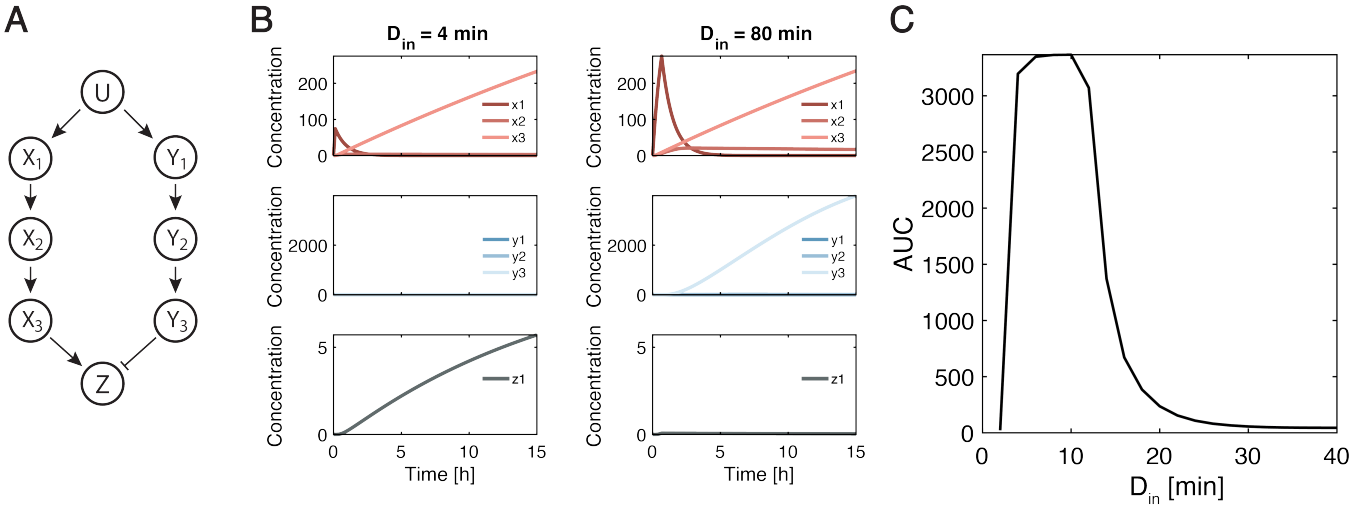

Figure 9: A GRN IFFL circuit showing the IDA property; the mathematical model is described in STAR Methods 3. (A) Diagram of the GRN IFFL circuit. (B) Dynamics of each node with $D_{in} = 4$ min (left) and $D_{in} = 80$ min (right). (C) AUC as a function of D_{in}, with parameters: $m = 3$, $n = 3$, $\delta_{x_1} = 20$, $\delta_{x_2} = 0.2$, $\delta_{x_3} = 0.3$, $\delta_{y_1} = 2.5$, $b_{y_2} = 45$, $\delta_{y_3} = 10$, $\delta_z = 0.01$, $\epsilon_{x_1} = 0.02$, $\epsilon_{x_2} = 0.0003$, $\epsilon_{x_3} = 0.0003$, $\epsilon_{y_1} = 0.0004$, $\epsilon_{y_2} = 0.004$, $\epsilon_{y_3} = 0.0003$, $\epsilon_z = 0.001$, $K_{x_1} = 0.5$, $K_{x_2} = 60$, $K_{x_3} = 0.6$, $K_{y_1} = 2.2$, $K_{y_2} = 5$, $K_{y_3} = 13$, $K_{xz} = 8$, $K_{yz} = 0.15$, $h_{x_1} = 2$, $h_{x_2} = 3$, $h_{x_3} = 3$, $h_{y_1} = 3$, $h_{y_2} = 4$, $h_{y_3} = 2$, $h_{xz} = 2$, $h_{yz} = 4$, $u = 0.5$.

Activation and inhibition rates on the output node affects IDA property

In the main text, we evaluated how the parameters of node X_i $(i = 1, ..., m)$ and Y_j $(i = 1, ..., n)$ affect the IDA property of generalized IFFL circuits. Here, we see how the output node parameters Z affect the IDA property of the same circuit motifs. Figure 10 shows three cases (different combinations of γ_j $(j = 1, ..., n)$) as evaluated in Section 3. For each case, eight different sets of $(\alpha_z,\ \beta_z)$ are evaluated. When we compare $\alpha_z = 10$ (top row) and $\alpha_z = 100$ (bottom row) for each case, $\alpha_z = 100$ gives broader areas with high IDA score for all the cases. These results suggest that, for obtaining a high IDA score, the output node has to be quickly activated during a relatively shorter period with a smaller D_{in}. Among four different values of β_z, $\beta_z = 1, 10$ give high IDA scores for case (B) and (C), while case (A) prefers $\beta_z = 10, 100$. These results supports the argument that relative balance of the activation and inhibition determines the IDA property, which was stated in the main text.

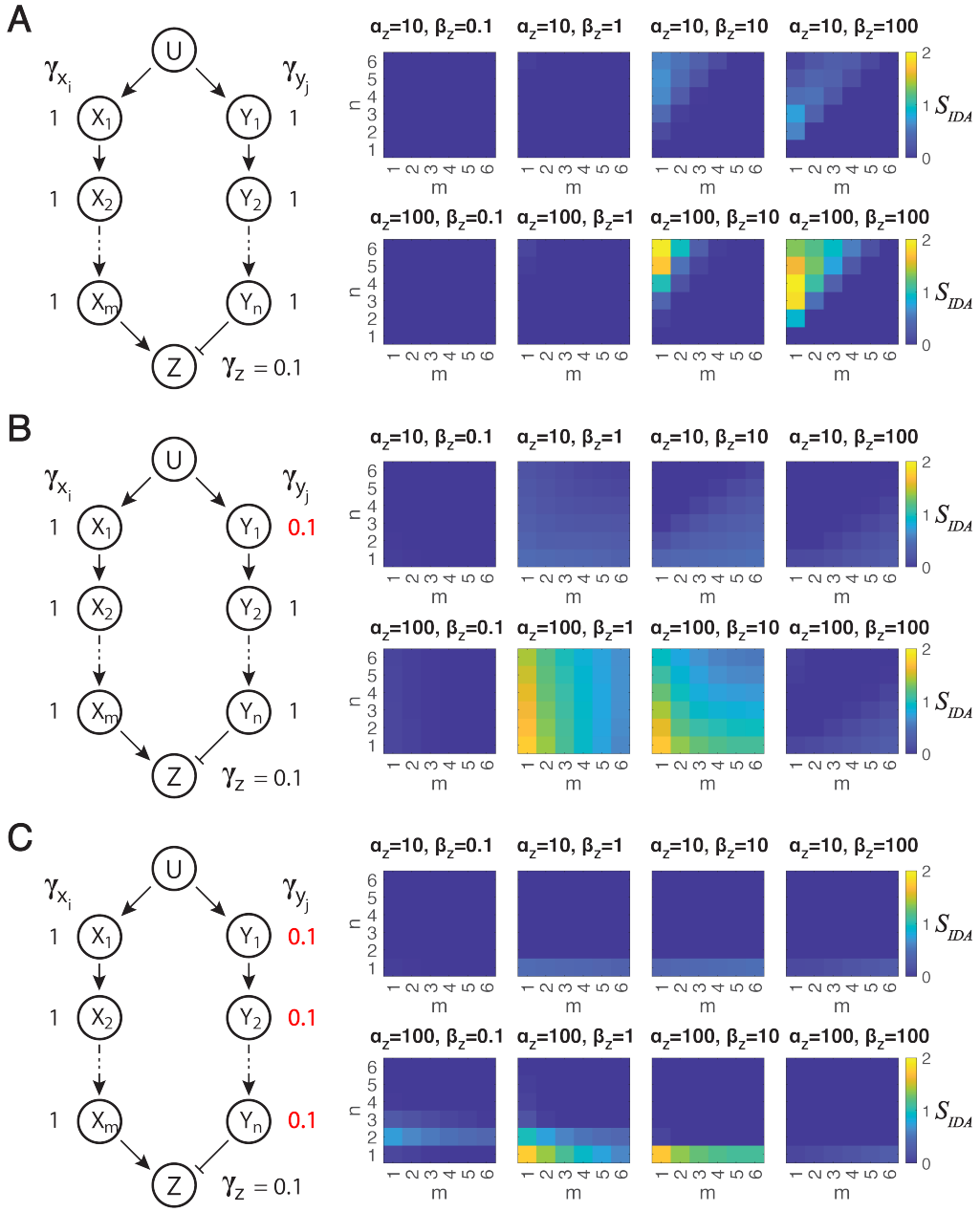

Figure 10: Parameters of the output node Z affects the IDA property of the generalized IFFL circuits. (A to C) Each panel shows the circuit diagram of a generalized IFFL network, along with heat maps of IDA scores S_{IDA} in the m-n plane for different values of α_z and β_z, reported above each heat map. The basal deactivation rates are reported next to each node in the circuit diagram: in all three cases, $\gamma_{x_i} = 1$ for all $i = 1, \ldots, m$, and moreover (A) $\gamma_{y_j} = 1$ for all $j = 1, \ldots, n$; (B) $\gamma_{y_1} = 0.1$, and $\gamma_{y_j} = 1$ for $j = 2, \ldots, n$; (C) $\gamma_{y_j} = 0.1$ for all $j = 1, \ldots, n$. When not varied, the parameters are kept constant at their nominal values: $\alpha_x = 1$, $\alpha_y = 1$, $\gamma_z = 0.1$, $K_{M,x} = K_{M,y} = K_{M,z} = 1.0$, $p_x = p_y = 1.0$, $p_z = 0.2$, $u_0 = 0.1$; D_{in} is logarithmically varied from $D_{in} = 0.1$ to $D_{in} = 10$.

Acknowledgments

E.N. and E.F acknowledge support from National Science Foundation through award NSF-CCF 2107483. F.B. has been partly supported by the Italian Ministry for Research in the framework of project Proliferation, Resistance and Infection Dynamics (PRIDE), PRIN 2022 by the European Union - NextGenerationEU grant no. 2022LP77J4; G.G. acknowledges support from the European Union through the ERC INSPIRE grant (project number 101076926); views and opinions expressed are however those of the authors only and do not necessarily reflect those of the European Union or the European Research Council; neither the European Union nor the granting authority can be held responsible for them. A.H. was supported by National Institutes of Health (R01AI173214). The authors thank all members of the labs for their support.

Author contributions

Conceptualization, E.N., A.H., and E.F.; mathematical model development, E.N., F.B., G.G., and E.F.; numerical simulations, E.N.; mathematical analysis, F.B., G.G., and E.F.; writing – original draft, E.N.; writing – review & editing, E.N., F.B., G.G, A.H., and E.F.; funding acquisition, E.F.; supervision, E.F.

Declaration of interests

The authors declare no competing interests.

References

1. Hoffmann, A., Levchenko, A., Scott, M. L., and Baltimore, D. (2002). The IκB-NF-κB signaling module: temporal control and selective gene activation. Science *298*, 1241–1245.

2. Purvis, J. E., and Lahav, G. (2013). Encoding and decoding cellular information through signaling dynamics. Cell *152*, 945–956.

3. Adelaja, A., Taylor, B., Sheu, K. M., Liu, Y., Luecke, S., and Hoffmann, A. (2021). Six distinct NFκB signaling codons convey discrete information to distinguish stimuli and enable appropriate macrophage responses. Immunity *54*, 916–930.e7.

4. Behar, M., and Hoffmann, A. (2010). Understanding the temporal codes of intra-cellular signals. Current opinion in genetics & development *20*, 684–693.

5. Gillies, T. E., Pargett, M., Minguet, M., Davies, A. E., and Albeck, J. G. (2017). Linear integration of ERK activity predominates over persistence detection in fra-1 regulation. Cell systems *5*, 549–563.e5.

6. Johnson, H. E., and Toettcher, J. E. (2019). Signaling dynamics control cell fate in the early drosophila embryo. Developmental cell *48*, 361–370.e3.

7. Uhlitz, F., Sieber, A., Wyler, E., Fritsche-Guenther, R., Meisig, J., Landthaler, M., Klinger, B., and Blüthgen, N. (2017). An immediate-late gene expression module decodes ERK signal duration. Molecular systems biology *13*, 928.

8. Panzeri, S., Brunel, N., Logothetis, N. K., and Kayser, C. (2010). Sensory neural codes using multiplexed temporal scales. Trends in neurosciences *33*, 111–120.

9. Walker, J. J., Terry, J. R., Tsaneva-Atanasova, K., Armstrong, S. P., McArdle, C. A., and Lightman, S. L. (2010). Encoding and decoding mechanisms of pulsatile hormone secretion. Journal of neuroendocrinology *22*, 1226–1238.

10. Dalkin, A. C., Haisenleder, D. J., Ortolano, G. A., Ellis, T. R., and Marshall, J. C. (1989). The frequency of gonadotropin-releasing-hormone stimulation differentially regulates gonadotropin subunit messenger ribonucleic acid expression. Endocrinology *125*, 917–924.

11. Stamatiades, G. A., and Kaiser, U. B. (2018). Gonadotropin regulation by pulsatile GnRH: Signaling and gene expression. Molecular and cellular endocrinology *463*, 131–141.

12. Ravindran, P. T., McFann, S., Thornton, R. H., and Toettcher, J. E. (2021). A synthetic gene circuit for imaging-free detection of signaling pulses. Cell systems.

13. Benzinger, D., Ovinnikov, S., and Khammash, M. (2022). Synthetic gene networks recapitulate dynamic signal decoding and differential gene expression. Cell systems *13*, 353–364.e6.

14. Lormeau, C., Rudolf, F., and Stelling, J. (2021). A rationally engineered decoder of transient intracellular signals. Nature communications *12*, 1886.

15. O'Brien, J., and Murugan, A. (2019). Temporal pattern recognition through analog molecular computation. ACS synthetic biology *8*, 826–832.

16. Zhang, C., Tsoi, R., Wu, F., and You, L. (2016). Processing oscillatory signals by incoherent feedforward loops. PLoS computational biology (1–16).

17. Luecke, S., Sheu, K. M., and Hoffmann, A. (2021). Stimulus-specific responses in innate immunity: Multilayered regulatory circuits. Immunity *54*, 1915–1932.

18. Mangan, S., Itzkovitz, S., Zaslaver, A., and Alon, U. (2006). The incoherent feed-forward loop accelerates the response-time of the gal system of escherichia coli. Journal of molecular biology *356*, 1073–1081.

19. Alon, U. (2007). Network motifs: Theory and experimental approaches. Nature reviews. Genetics *8*, 450–461.

20. Schaffter, S. W., Chen, K.-L., O'Brien, J., Noble, M., Murugan, A., and Schulman, R. (2022). Standardized excitable elements for scalable engineering of far-from-equilibrium chemical networks. Nature chemistry.

21. Ryan, J., Hong, S., Foo, M., Kim, J., and Tang, X. (2022). Model-based investigation of the relationship between regulation level and pulse property of I1-FFL gene circuits. ACS synthetic biology *11*, 2417–2428.

22. Westbrook, A., Tang, X., Marshall, R., Maxwell, C. S., Chappell, J., Agrawal, D. K., Dunlop, M. J., Noireaux, V., Beisel, C. L., Lucks, J., and Franco, E. (2019). Distinct timescales of RNA regulators enable the construction of a genetic pulse generator. Biotechnology and bioengineering *116*, 1139–1151.

23. Basu, S., Mehreja, R., Thiberge, S., Chen, M. T., Weiss, R., and Modeling, D. (2004). Spatiotemporal control of gene expression with pulse-generating networks. Proceedings of the National Academy of Sciences of the United States of America *101*, 6355–6360.

24. Guo, S., and Murray, R. M. (2019). Construction of incoherent feedforward loop circuits in a cell-free system and in cells. ACS synthetic biology *8*, 606–610.

25. Sontag, E. D. (2010). Remarks on feedforward circuits, adaptation, and pulse memory. IET systems biology *4*, 39–51.

26. Goentoro, L., Shoval, O., Kirschner, M. W., and Alon, U. (2009). The incoherent feedforward loop can provide fold-change detection in gene regulation. Molecular cell *36*, 894–899.

27. Shoval, O., Alon, U., and Sontag, E. (2011). Symmetry invariance for adapting biological systems. SIAM journal on applied dynamical systems *10*, 857–886.

28. Basu, S., Gerchman, Y., Collins, C. H., Arnold, F. H., and Weiss, R. (2005). A synthetic multicellular system for programmed pattern formation. Nature *434*, 1130–1134.

29. Greber, D., and Fussenegger, M. (2010). An engineered mammalian band-pass network. Nucleic acids research *38*, e174.

30. Takahashi, J. S. (2017). Transcriptional architecture of the mammalian circadian clock. Nature reviews. Genetics *18*, 164–179.

31. Mitchell, S., Vargas, J., and Hoffmann, A. (2016). Signaling via the NFκB system. Wiley interdisciplinary reviews. Systems biology and medicine *8*, 227–241.

32. Batchelor, E., Mock, C. S., Bhan, I., Loewer, A., and Lahav, G. (2008). Recurrent initiation: a mechanism for triggering p53 pulses in response to DNA damage. Molecular cell *30*, 277–289.

33. Shoval, O., Goentoro, L., Hart, Y., Mayo, A., Sontag, E., and Alon, U. (2010). Fold-change detection and scalar symmetry of sensory input fields. Proceedings of the National Academy of Sciences of the United States of America *107*, 15995–16000.

34. Adler, M., Szekely, P., Mayo, A., and Alon, U. (2017). Optimal regulatory circuit topologies for fold-change detection. Cell Systems *4*, 171–181.e8.

35. Ma, W., Trusina, A., El-Samad, H., Lim, W. A., and Tang, C. (2009). Defining network topologies that can achieve biochemical adaptation. Cell *138*, 1–55.

36. Aoki, S. K., Lillacci, G., Gupta, A., Baumschlager, A., Schweingruber, D., and Khammash, M. (2019). A universal biomolecular integral feedback controller for robust perfect adaptation. Nature *570*, 533–537.

37. Mangan, S., and Alon, U. (2003). Structure and function of the feed-forward loop network motif. Proceedings of the National Academy of Sciences of the United States of America *100*, 11980–11985.

38. Tyson, J. J., Chen, K. C., and Novak, B. (2003). Sniffers, buzzers, toggles and blinkers: dynamics of regulatory and signaling pathways in the cell. Current opinion in cell biology *15*, 221–231.

39. Wall, M. E., Dunlop, M. J., and Hlavacek, W. S. (2005). Multiple functions of a feed-forward-loop gene circuit. Journal of molecular biology *349*, 501–514.

40. Gerardin, J., Lim, W. A., Reddy, N. R., and Lim, W. A. (2019). The design principles of biochemical timers: Circuits that discriminate between transient and sustained stimulation - supplemental. Cell Systems *9*, 297–308.e2.

41. Tzafriri, A. R., and Edelman, E. R. (2004). The total quasi-steady-state approximation is valid for reversible enzyme kinetics. Journal of theoretical biology *226*, 303–313.

42. Ackers, G. K., Johnson, A. D., and Shea, M. A. (1982). Quantitative model for gene regulation by lambda phage repressor. Proceedings of the National Academy of Sciences of the United States of America *79*, 1129–1133.

43. Yu, P. Y., and Sontag, E. D. (2024). A necessary condition for non-monotonic dose response, with an application to a kinetic proofreading model – extended version. arXiv [q-bio.MN].

44. Gao, X. J., Chong, L. S., Kim, M. S., and Elowitz, M. B. (2018). Programmable protein circuits in living cells. Science (New York, N.Y.) *361*, 1252–1258.

45. Shui, S., Scheller, L., and Correia, B. E. (2023). Protein-based bandpass filters for controlling cellular signaling with chemical inputs. Nature chemical biology.

46. Levine, J. H., Lin, Y., and Elowitz, M. B. (2013). Functional roles of pulsing in genetic circuits. Science *342*, 1193–1200.

47. Lee, R. E. C., Qasaimeh, M. A., Xia, X., Juncker, D., and Gaudet, S. (2016). NFκB signalling and cell fate decisions in response to a short pulse of tumour necrosis factor. Scientific reports *6*, 39519.

48. Dupin, A., and Simmel, F. C. (2019). Signalling and differentiation in emulsion-based multi-compartmentalized in vitro gene circuits. Nature chemistry *11*, 32–39.

49. Aubert-Kato, N., and Cazenille, L. (2020). Designing dynamical molecular systems with the pen toolbox. New Generation Computing *38*, 341–366.

50. Gordley, R. M., Williams, R. E., Bashor, C. J., Toettcher, J. E., Yan, S., and Lim, W. A. (2016). Engineering dynamical control of cell fate switching using synthetic phospho-regulons. Proceedings of the National Academy of Sciences of the United States of America *113*, 13528–13533.

51. Yang, X., Rocks, J. W., Jiang, K., Walters, A. J., Rai, K., Liu, J., Nguyen, J., Olson, S. D., Mehta, P., Collins, J. J., Daringer, N. M., and Bashor, C. J. (2023). Engineering synthetic phosphorylation signaling networks in human cells. bioRxiv (2023.09.11.557100).

52. Gong, X., Wei, J., Liu, J., Li, R., Liu, X., and Wang, F. (2019). Programmable intracellular DNA biocomputing circuits for reliable cell recognitions. Chemical science (Royal Society of Chemistry: 2010) *10*, 2989–2997.

53. Lienert, F., Lohmueller, J. J., Garg, A., and Silver, P. A. (2014). Synthetic biology in mammalian cells: next generation research tools and therapeutics. Nature reviews. Molecular cell biology *15*, 95–107.

54. Kumar, S., and Khammash, M. (2022). Platforms for optogenetic stimulation and feedback control. Frontiers in bioengineering and biotechnology *10*, 918917.

55. Heinrich, R., Neel, B. G., and Rapoport, T. A. (2002). Mathematical models of protein kinase signal transduction. Molecular cell *9*, 957–970.

STAR METHODS

Resource availability

Lead contact

Requests for further information and resources should be directed to and will be fulfilled by the lead contact, Elisa Franco (efranco@seas.ucla.edu).

Materials availability

This study did not generate new materials.

Data and code availability

- All the numerical simulation data used for the figures are publicly available as of the date of publication at https://github.com/enaka74/IDR.
- All original code has been deposited at https://github.com/enaka74/IDR and is publicly available as of the date of publication.
- Any additional information required to reanalyze the data reported in this paper is available from the lead contact upon request.

Method details

Mathematical models for the negative feedback loop (NFL) circuit

Temporarily denoting the concentration of species Y as $\bar{y}$, we introduce the simple NFL model as follows:

$$\frac{dx(s)}{ds} = \alpha\bar{y}(s) - \beta x(s) \tag{18}$$

$$\frac{d\bar{y}(s)}{ds} = \gamma u(s) - \delta x^p(s)\bar{y}(s) - \epsilon\bar{y}(s) \tag{19}$$

where α and γ are the activation rate constants for species X and Y respectively; β and ϵ are the self-degradation rate constants for species X and Y respectively; δ is the rate constant associated with inhibition of Y mediated by X, and p represents the order (i.e., cooperativity) of the reaction, while s is the time variable. To reduce the number of parameters, we rescale time in Equations 18 and 19 and obtain the new ODE model, which we will analyze in the following without loss of generality:

$$\dot{x}(t) = y(t) - x(t) \tag{20}$$

$$\dot{y}(t) = au(t) - bx^p(t)y(t) - cy(t) \tag{21}$$

where $t = \beta s$, $y = \alpha\bar{y}/\beta$, $a = \gamma/\beta$, $b = \delta/\alpha$, $c = \epsilon\beta/\alpha$, while $\dot{x}(t) = \frac{dx(t)}{dt}$ and $\dot{y}(t) = \frac{dy(t)}{dt}$. Note that variable y is rescaled here. Using Equations 20 and 21, we can evaluate the circuit dynamics with respect to a, b, c, and p, as done in the main text.

The signaling model of NFL is as follows:

$$\dot{x}(t) = \alpha_x \frac{y(t)[1-x(t)]}{K_{M,yx} + y(t) + [1-x(t)]} - \gamma_x \frac{p_x x(t)}{K_{M,px} + p_x + x(t)} \tag{22}$$

$$\dot{y}(t) = \alpha_y \frac{u(t)[1-y(t)]}{K_{M,uy} + u(t) + [1-y(t)]} - \beta_y \frac{x(t)y(t)}{K_{M,xy} + x(t) + y(t)} - \gamma_y \frac{p_y}{K_{M,py} + p_y + y(t)} \tag{23}$$

The gene regulatory model of NFL is as follows:

$$\dot{x}(t) = \delta_x \frac{[u(t)/K_{D,ux}]^{h_{ux}}}{1 + [u(t)/K_{D,ux}]^{h_{ux}}} - \epsilon_x x(t) \tag{24}$$

$$\dot{y}(t) = \delta_y \frac{[u(t)/K_{D,uy}]^{h_{uy}}}{1 + [u(t)/K_{D,uy}]^{h_{uy}} + [x(t)/K_{D,xy}]^{h_{xy}}} - \epsilon_y y(t) \tag{25}$$

The parameters for each model are defined in the same way as those for IFFL.

Gene regulatory network model for the generalized incoherent feedforward loop (IFFL) circuit

We consider the following gene regulatory network model for the generalized incoherent feedforward loop:

$$\dot{x}_1(t) = \delta_{x_1} \frac{[u(t)/K_{D,ux}]^{h_{ux}}}{1 + [u(t)/K_{D,ux}]^{h_{ux}}} - \epsilon_{x_1} x_1(t) \tag{26}$$

$$\dot{y}_1(t) = \delta_{y_1} \frac{[u(t)/K_{D,uy}]^{h_{uy}}}{1 + [u(t)/K_{D,uy}]^{h_{uy}}} - \epsilon_{y_1} y_1(t) \tag{27}$$

$$\dot{x}_i(t) = \delta_{x_i} \frac{[x_{i-1}(t)/K_{D,x_i}]^{h_{x_i}}}{1 + [x_{i-1}(t)/K_{D,x_i}]^{h_{x_i}}} - \epsilon_{x_i} x_i(t) \quad (i = 2, ..., m) \tag{28}$$

$$\dot{y}_j(t) = \delta_{y_j} \frac{[y_{j-1}(t)/K_{D,y_j}]^{h_{y_j}}}{1 + [y_{j-1}(t)/K_{D,y_j}]^{h_{y_j}}} - \epsilon_{y_j} y_j(t) \quad (j = 2, ..., n) \tag{29}$$

$$\dot{z}(t) = \delta_z \frac{[x_m(t)/K_{D,xz}]^{h_{xz}}}{1 + [x_m(t)/K_{D,xz}]^{h_{xz_1}} + [y_n(t)/K_{D,yz}]^{h_{yz}}} - \epsilon_z z(t) \tag{30}$$

where δ is the activation rate and ϵ is the dilution/degradation rate for an expressed protein, while K_D is the dissociation constant of a transcription factor on its target promoter. The subscripts indicate the species in which a constant is involved; for example, δ_{x_i} is the activation rate of X and K_{D,y_j} is the dissociation constant between the transcription factor expressed from the gene Y_{j-1} and the targeted promoter for gene Y_j.

Quantification of the inverse properties

We introduce several mathematical formulae from Heinrich's work[55] to evaluate the transient dynamics of a signal. With the formulae, we can quantify temporal features of a signal of an arbitrary shape. Given the function $f(t)$ of time, which can be the temporal signal obtained as the output response of a biological circuit, the formulae are as follows.

$$I = \int_0^\infty f(t)dt \tag{31}$$

$$T = \int_0^\infty t f(t)dt \tag{32}$$

$$\tau = T/I \tag{33}$$

$$Q = \int_0^\infty t^2 f(t)dt \tag{34}$$

$$D_{out} = \sqrt{Q/I - (T/I)^2} \tag{35}$$

I is the integral of the signal, also referred to as the area under the curve or AUC, i.e. the integrated response. T is the time-weighted integrated response, while the *signaling time* τ is the average time required to activate the response. Q is the squared-time-weighted integrated response. The signal duration is denoted by D_{out}. The quantities τ and D_{out} are analogous to the mean and standard deviation, respectively, of a continuous statistical distribution. Throughout the present study, we evaluate the signal

duration of an output response by computing D_{out} as in Equation 35. It should be noted that D_{out} is undefined when $f(t) = 0$ due to division by zero. Specifically, $D_{in} = 0$ results in no response across all the models evaluated in the main text. Therefore, $D_{out}(D_{in} = 0)$ is not considered in this study.
Next we define and quantify the IDD property. We suppose $D_{out}(D_{in})$, namely the output signal duration as a function of the input signal duration, can have an arbitrary functional form, as shown in Fig. 11. The steps to compute the IDD score S_{IDD} are as follows: First, we locate all the local maxima, D_{out,M_i}, and local minima, D_{out,m_j}. D_{in,M_i} and D_{in,m_j} are the input pulse durations that give D_{out,M_i} and D_{out,m_j} (i.e., $D_{out,M_i} = D_{out}(D_{in,M_i})$, $D_{out,m_j} = D_{out}(D_{out,m_j})$). Next we consider all combinations of D_{out,M_i} and D_{out,m_j}. Finally, we determine the combination that gives the maximum value of $\frac{D_{out,M_i}}{D_{out,m_j}} - 1$, satisfying $D_{out,M_i} < D_{out,m_j}$, which guarantees the IDD property is maintained for all $D_{M,i} \leq D_{in} \leq D_{m,j}$. The following definition mathematically represents the IDD score S_{IDD} determined through the above steps:

$$S_{ij} = \frac{D_{out,M_i}}{D_{out,m_j}} - 1 \quad (i = 1, ..., N_M, j = 1, ..., N_m) \tag{36}$$

$$S_{IDD} = max\{S_{ij} \quad s.t. \quad D_{M,i} < D_{m,j}\} \tag{37}$$

where N_M and N_m are the total number of maxima and minima, respectively. If $D_{out}(D_{in})$ is a non-decreasing function, then S_{IDD} is defined as zero. Because a constant function can be considered to have $D_{out,M} = D_{out,m}$, which gives $S_{IDD} = 0$, this extension of the definition is reasonable. This expression can quantify the IDD property of an arbitrary shape of $D_{out}(D_{in})$ curve. Based on this definition, if a response has an interval of D_{in} values for which $D_{out}(D_{in})$ locally decreases, the response has a positive S_{IDD}; otherwise, $S_{IDD} = 0$. An IDA score S_{IDA} is calculated in the same way, just considering function $I(D_{in})$, namely $AUC(D_{in})$.

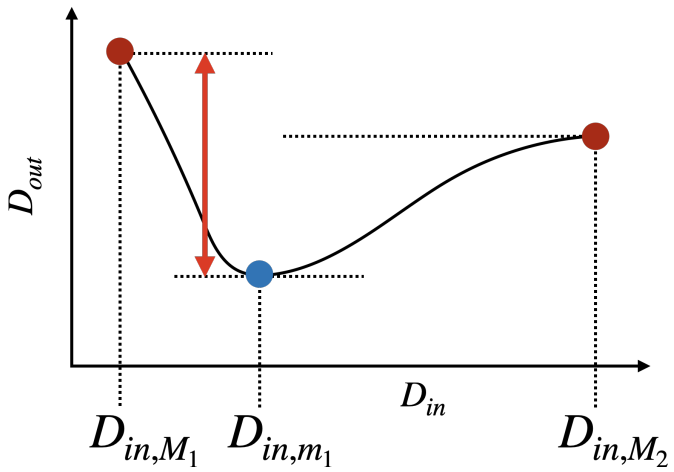

Figure 11: A schematic example of function $D_{out}(D_{in})$ and steps to find the $(D_{out,M_i}, D_{out,m_j})$ pair to compute the IDD score.

Computational simulations and random parameter sampling for the biological network models

All the numerical simulations were performed using MATLAB. The ode23s solver was used for the signaling models, and the ode15s solver was used for the GRN models. For random parameter sampling, each parameter (except for the Hill coefficient h) was sampled from the uniform distribution in the interval specified by the lower and upper limits listed in Table 1 using the MATLAB $rand$ function. The Hill coefficient was sampled from the discrete uniform distribution on the interval specified by the lower and upper limits, as shown in Table 1.

Table 1: Parameter ranges for the random parameter sampling.

Parameter	Unit	Lower limit	Upper limit
α	min^{-1}	1	100
β	min^{-1}	1	100
γ	min^{-1}	1	100
K_M	μM	1	1000
P	μM	0.1	1
δ	μM	0.1	100
ϵ	μM	0.1	100
h	-	1	4